Available online at www.sciencedirect.com
ScienceDirect
Journal of Computational Physics 227 (2007) 1225–1245
JOURNAL OF COMPUTATIONAL PHYSICS
www.elsevier.com/locate/jcp

Near-field performance analysis of locally-conformal perfectly matched absorbers via Monte Carlo simulations

Ozlem Ozgun *, Mustafa Kuzuoglu

Department of Electrical and Electronics Engineering, Middle East Technical University, 06531 Ankara, Turkey

Received 7 January 2007; received in revised form 14 June 2007; accepted 31 August 2007
Available online 11 September 2007

Abstract

In the numerical solution of some boundary value problems by the finite element method (FEM), the unbounded domain must be truncated by an artificial absorbing boundary or layer to have a bounded computational domain. The perfectly matched layer (PML) approach is based on the truncation of the computational domain by a reflectionless artificial layer which absorbs outgoing waves regardless of their frequency and angle of incidence. In this paper, we present the near-field numerical performance analysis of our new PML approach, which we call as locally-conformal PML, using Monte Carlo simulations. The locally-conformal PML method is an easily implementable conformal PML implementation, to the problem of mesh truncation in the FEM. The most distinguished feature of the method is its simplicity and flexibility to design conformal PMLs over challenging geometries, especially those with curvature discontinuities, in a straightforward way without using artificial absorbers. The method is based on a special complex coordinate transformation which is 'locally-defined' for each point inside the PML region. The method can be implemented in an existing FEM software by just replacing the nodal coordinates inside the PML region by their complex counterparts obtained via complex coordinate transformation. We first introduce the analytical derivation of the locally-conformal PML method for the FEM solution of the two-dimensional scalar Helmholtz equation arising in the mathematical modeling of various steady-state (or, time-harmonic) wave phenomena. Then, we carry out its numerical performance analysis by means of some Monte Carlo simulations which consider both the problem of constructing the two-dimensional Green's function, and some specific cases of electromagnetic scattering.

Keywords: Helmholtz equation; Finite element method (FEM); Perfectly matched layer (PML); Mesh truncation; Complex coordinate stretching

1. Introduction

The finite element method (FEM) is a numerical method developed for the approximate solution of boundary value problems governed by partial differential equations, arising in various fields of science and engineering

* Corresponding author. Tel.: +90 312 210 23 73; fax: +90 312 210 12 61.
E-mail address: ozgunozlem@gmail.com (O. Ozgun).

0021-9991/$ - see front matter © 2007 Elsevier Inc. All rights reserved.
doi:10.1016/j.jcp.2007.08.025

(such as elasticity, electromagnetics, mechanics, acoustics, seismology and geophysics). The method is of great interest for scientists and engineers due to its flexibility in modeling complicated problems defined on spatial domains having irregular boundaries and arbitrary domain properties. The most distinctive feature of the FEM is the decomposition of a given domain into a set of simple domains, called finite elements. The computational domain (i.e., the FEM mesh) is then considered as an assembly of these elements connected at a finite number of preselected points, called nodes. Over each element, an approximation to the solution is expressed as a linear combination of nodal values and approximation functions (i.e., shape functions). Then, the local algebraic relations are derived among the nodal values of the solution over each element, and assembled to obtain the global equation system whose solution yields the nodal values of the unknown function.

In the numerical modeling of several problems, especially wave propagation problems arising in the above mentioned fields, the physical domain extends to infinity. Electromagnetic radiation or scattering, acoustic wave propagation, seismic wave propagation and elastic wave propagation are examples of some application areas, where wave propagation occurs in unbounded domains. In order to employ the FEM to the solution of such problems involving spatially unbounded domains, the physical domain must be truncated by an artificial boundary or layer to achieve a bounded computational domain. A popular approach to the mesh truncation problem is the introduction of a reflectionless absorbing layer, which is called the perfectly matched layer (PML), at the outer boundary. The PML concept has been first introduced by Berenger [1] in the context of the finite difference time domain method (FDTD) for the numerical approximation of problems governed by Maxwell's equations. Berenger's PML is based on a split-field formulation of Maxwell's equations in Cartesian coordinates, and yields non-Maxwellian fields within the PML domain. In the context of time-harmonic wave propagation, the PML approach is basically the truncation of the computational domain by an artificial layer which absorbs outgoing plane waves irrespective of their frequency and angle of incidence, without any reflection. The most attractive feature of the PML is the ability to minimize the white space due to its close proximity and conformity to the surface of the object.

Following the introduction of the PML in the FDTD method, the PML concept has been used extensively in FDTD applications [2–4]. A major step, which may be considered as a touchstone to start the implementation of the PML in the FEM simulations, is achieved by Sacks et al. [5], who constructed a Maxwellian PML in Cartesian coordinates as an 'anisotropic layer' with appropriately defined permittivity and permeability tensors. The anisotropic PML concept, originally introduced in Cartesian coordinates, has been extended to cylindrical and spherical coordinates [6], and has been used in the design of conformal PMLs using a local curvilinear coordinate system [7]. The PML approach, based on either the Berenger's formulation or the anisotropic formulation, has been successfully applied in many other fields, e.g. acoustics [8,9]; elasticity [10,11]; linearized Euler equations [12,13]; eddy current problems [14]; and wave propagation in poroelastic media [15].

Another formulation, yielding a PML action, has been introduced by Chew and Weedon [16] for use in the FDTD method. This non-Maxwellian approach is implemented via the concept of complex coordinate stretching, which is essentially the analytical continuation of the field variables to complex space. However, in FEM applications, a PML realized by complex coordinate stretching has been interpreted as an anisotropic PML in cylindrical, spherical [17], and curvilinear coordinates [18]. This is achieved through the mapping of the non-Maxwellian fields obtained during the complex coordinate transformation to a set of Maxwellian fields in an anisotropic medium representing the PML.

All of the previous PML realizations in FEM literature employ artificial absorbing materials and utilize a local/nonlocal coordinate system in order to design the PML as an 'anisotropic medium' having suitably defined constitutive parameters. However, in this paper we present an analysis of the new ''locally-conformal PML'' approach, which does not need any artificial materials or coordinate system, for mesh truncation in FEM applications (clearly, the method is non-Maxwellian in the context of electromagnetics, since the avoidance of artificial material layers leads to field expressions that do not satisfy Maxwell's equations). Although we have previously introduced the underlying concept of this approach in [19] for the solution of three-dimensional electromagnetic vector wave equation using edge elements, we have dealt with only the far-field performance of this method in terms of the radar cross section (RCS) calculations. It is evident that the smoothing effect of the far-field calculation may result in a reduction in the magnitude of errors present in the near field terms. In this paper, therefore, we perform an extensive numerical investigation of the near-field accuracy of

the proposed method using the Monte Carlo simulation technique for the solution of two-dimensional (2D) scalar Helmholtz equation using nodal elements. It is well known that, various problems related to steady-state oscillations (mechanical, acoustical, thermal, electromagnetic) lead to the 2D Helmholtz equation. In other words, the scope of the Helmholtz equation is broad due to its relationship to the wave equation in sinusoidal steady-state. Therefore, although the analysis of the method is presented in conjunction with problems in electromagnetism, the proposed method is applicable in the above mentioned areas in a straightforward manner.

The locally-conformal PML method is based on a ''locally-defined'' complex coordinate transformation. Although the concept of coordinate transformation has long been utilized in the context of PMLs, the true novelty in the locally-conformal PML method is the 'definition of the transformation', which is locally-defined and which does not explicitly depend on the differential geometric properties of the PML-free space interface. In other words, the locally-conformal PML utilizes a special type of complex coordinate stretching, which differs from all previous coordinate transformations in FEM literature. The locally-conformal PML has some vital practical advantages from the point of view of the easy design of PMLs having challenging geometries, especially having some intersection regions or abrupt changes in curvature. Although the anisotropic PML has been used in the 'conceptual' design of conformal PMLs via a local coordinate system [7,18], this approach exhibits some difficulties in terms of the computational and analytical effort, especially for the implementation of the PML in the case of curvature discontinuities. Likewise, a majority of PML realizations in numerical FEM applications have been implemented in a rectangular or circular PML domain, which does not have arbitrary curvature discontinuities. The major advantage of the present approach is its flexibility to design a conformal PML domain which encloses an arbitrarily-shaped convex spatial domain. Such conformal PML domains are very crucial especially in wave propagation problems, where the minimization of the white space is essential in order to save on the computational supply (such as memory and processing power).

In the locally-conformal PML method, the analytic continuation of the frequency-domain waves to complex space, via the complex coordinate transformation, yields a PML region which absorbs outgoing waves without any reflection. The locally-conformal PML is designed in complex space by just replacing the real coordinates with their complex counterparts calculated in terms of the special complex coordinate transformation. Its implementation is simply based on the parametric representation of the complex coordinate transformation defined in terms of only a few parameters, which are easily derived from the node coordinates in an existing FEM mesh using some very simple search techniques. In this formulation, the weak variational form of the governing differential equation is derived in terms of the complex coordinates. Then, the weak variational form of the differential equation is discretized using the complex elements (i.e., elements with complex nodal coordinates). In other words, the elements in the real coordinate system are mapped to the complex elements in complex space, through the complex coordinate stretching. Since the algebraic equations related to the FEM formulation in PML region depend directly on the nodal coordinates, the replacement of the node coordinates with the complex coordinates is sufficient to achieve the realization of the locally-conformal PML.

The structure of this paper is as follows: In Section 2, we briefly derive the equations governing the parametric construction of the locally-conformal PML method designed over an arbitrarily-shaped convex spatial domain. Section 3 formulates the FEM in complex PML space using triangular isoparametric elements for the solution of the 2D scalar Helmholtz equation in complex space. In Section 4, we present several numerical applications involving both the problem of constructing the 2D free-space Green's function and the electromagnetic scattering problem, in order to illustrate the near-field accuracy of the locally-conformal PML approach in the FEM mesh truncation. In the construction of the 2D Green's function, we utilize the Monte Carlo simulation technique for the purpose of more reliable numerical performance analysis of the locally-conformal PML method. Finally, we draw some conclusions in Section 5.

2. Parametric construction of the locally-conformal PML method

The locally-conformal PML method is based on a locally-defined complex coordinate transformation [19]. As a starting point of the technique, we spatially construct the PML region (Ω_{PML}) as conformal to an arbitrary source volume containing sources of waves and obstacles. The source volume can be chosen as the convex hull (i.e., the smallest convex set that encloses the sources and obstacles) to minimize the computational

domain. For the sake of illustrating the method, we consider the geometries in Fig. 1 which represent arbitrary partial cross-sections of the PML region enclosed within the boundaries $\partial\Omega_{\text{in}}$ and $\partial\Omega_{\text{out}}$.

In the locally-conformal PML method, we define the complex coordinate transformation, which maps each point P in Ω_{PML} to $\widetilde{P}$ in complex PML region $\Gamma \subset C^2$, as follows [19] (assuming a suppressed time-dependence $e^{j\omega t}$):

$$\tilde{\vec{r}} = \vec{r} + \frac{1}{jk} f(\xi)\hat{n}(\xi), \tag{1}$$

where $\vec{r} \in \Re^2$ and $\tilde{\vec{r}} \in C^2$ are the position vectors of the points P in real space and $\widetilde{P}$ in complex space, respectively; $k = \omega/\upsilon$ represents the wave number (ω is the angular frequency, υ is the velocity of propagation); ξ is the parameter defined by $\xi = \|\vec{r} - \vec{r}_{\text{in}}\|$; and $\vec{r}_{\text{in}} \in \partial\Omega_{\text{in}}$ is the position vector of the point P_{in} located on $\partial\Omega_{\text{in}}$ (see Fig. 1), which is the solution of the minimization problem: $\min_{\vec{r}_{\text{in}} \in \partial\Omega_{\text{in}}} \|\vec{r} - \vec{r}_{\text{in}}\|$ which yields a unique $\vec{r}_{\text{in}}$ because $\partial\Omega_{\text{in}}$ is the boundary of the convex set, and which can be simply performed by using some search techniques in the mesh coordinates of the existing FEM program. Furthermore, $\hat{n}(\xi)$ is the unit vector defined by $\hat{n}(\xi) = (\vec{r} - \vec{r}_{\text{in}})/\xi$, and $f(\xi)$ is a monotonically increasing function of ξ as follows:

$$f(\xi) = \frac{\alpha \xi^m}{m\|\vec{r}_{\text{out}} - \vec{r}_{\text{in}}\|^{m-1}}, \tag{2}$$

where α is a positive parameter, m is a positive integer (typically 2 or 3) related to the decay rate of the magnitude of the wave inside Ω_{PML}, and $\vec{r}_{\text{out}}$ is the position vector of the point P_{out} which is basically the intersection of the line passing through $\vec{r}$ and $\vec{r}_{\text{in}}$ (i.e., the dotted line in Fig. 1) and $\partial\Omega_{\text{out}}$. In Eq. (2), $\|\vec{r}_{\text{out}} - \vec{r}_{\text{in}}\|$ represents the local PML thickness (d_{PML}) for the corresponding PML point. The exponents in Eq. (2) are chosen in such a way that m is in the numerator and $m - 1$ is in the denominator, because of possible simplifications in the derivative terms of the Jacobian matrix appearing in the complex coordinate transformation. The transformation in Eq. (1) induces a smooth exponential decay of the transmitted wave inside Ω_{PML} along the direction of the unit vector, provided that the values of the PML parameters (d_{PML}, α and m) are chosen properly, as demonstrated numerically in Section 4.2.1. More explicitly, Eq. (1) in conjuction with Eq. (2) meets the following three conditions which should be satisfied for a successful PML realization:

(i) the outgoing wave in the neighborhood of the point P_{in} must be transmitted into Ω_{PML} without any reflection,
(ii) the transmitted wave must be subject to a monotonic decay within Ω_{PML},
(iii) the magnitude of the transmitted wave must be negligible on $\partial\Omega_{\text{PML}}$.

In the Appendix, we demonstrate that these conditions are satisfied for a scalar outgoing wave under the coordinate transformation given in Eq. (1).

It is evident that the calculation of the PML parameters appearing in Eq. (1) is local in the sense that each PML point has its own parameters depending on its position inside the PML region. If the point $\vec{r}_{\text{in}}$ is located on $\partial\Omega_{\text{in}}$ whose curvature is continuous (see Fig. 1a), the unit vector $\hat{n}(\xi)$ is obviously the unit vector which is

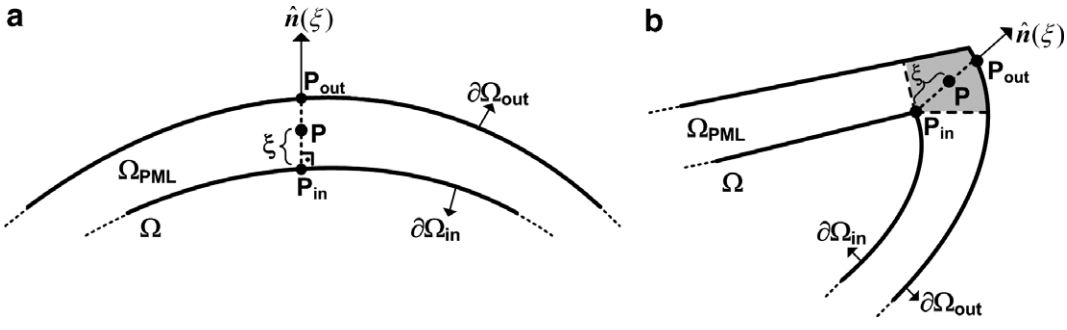

Fig. 1. Locally-conformal PML implementation: (a) PML region with smooth curvature, (b) PML region with curvature discontinuity.

normal to $\partial\Omega_{\text{in}}$. However, for PML points located inside the intersection region (close to the curvature discontinuity) which is gray-shaded in Fig. 1b, the solution of the minimization problem results in the same value for $\vec{r}_{\text{in}}$. In both cases, the implementations of the transformation in Eq. (1) in an ordinary FEM program are identical owing to a single algorithm performing the task which replaces the real coordinates inside the PML region with their complex counterparts calculated by the complex coordinate transformation in Eq. (1). Since the coordinate transformation is locally-defined without using any coordinate system, the geometry of $\partial\Omega_{\text{in}}$ is not important for the application of the method and the transformation yields analytic continuity even in the case of curvature discontinuities on $\partial\Omega_{\text{in}}$.

It should be obvious that the definition of the complex coordinate stretching in Eq. (1) is not arbitrary, and should satisfy some certain criteria [enumerated by (i), (ii), (iii) above] for an efficient PML design. One can claim that other complex coordinate transformations can also be defined similarly for the PML design. For example, if we define the stretching operation as shown in Fig. 2 by omitting the minimization problem and calculating the PML parameters according the unit vector $\hat{a}_\xi$ emanating from a center point P_{c} in the direction of the PML point, then this complex coordinate transformation fails (i.e. the resulting PML design is not successful) when $\theta > 45°$ [20]. Thus, the transformation in Eq. (1) in the locally-conformal PML method is a specifically-defined complex stretching operation to design effectively a PML domain which encloses an arbitrarily-shaped convex spatial domain.

Classical cartesian and cylindrical PML approaches in FEM literature which are usually realized in the design of PMLs over rectangular and circular regions, respectively, are actually the special cases of the locally-conformal PML method in terms of the complex coordinate transformation. For instance, if the PML region surrounds a rectangular spatial domain as shown in Fig. 3a, the classical cartesian PML approach considers the following definition of the transformation:

$$\tilde{x} = x + \frac{\alpha}{\mathrm{j}k}(x - x_{\text{in}}), \quad \tilde{y} = y \text{ (in region I)}, \tag{3a}$$

$$\tilde{y} = y + \frac{\alpha}{\mathrm{j}k}(y - y_{\text{in}}), \quad \tilde{x} = x \text{ (in region II)}, \tag{3b}$$

$$\tilde{x} = x + \frac{\alpha}{\mathrm{j}k}(x - x_{\text{in}}), \quad \tilde{y} = y + \frac{\alpha}{\mathrm{j}k}(y - y_{\text{in}}) \text{ (in region III)}. \tag{3c}$$

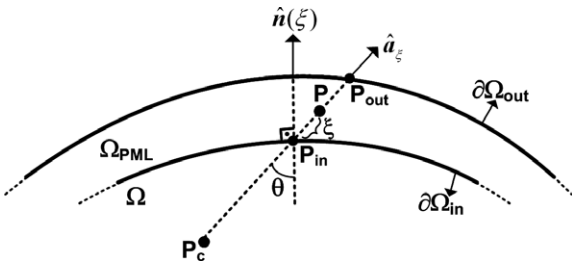

Fig. 2. Modified locally-conformal PML implementation with respect to a center (fails when $\theta > 45°$).

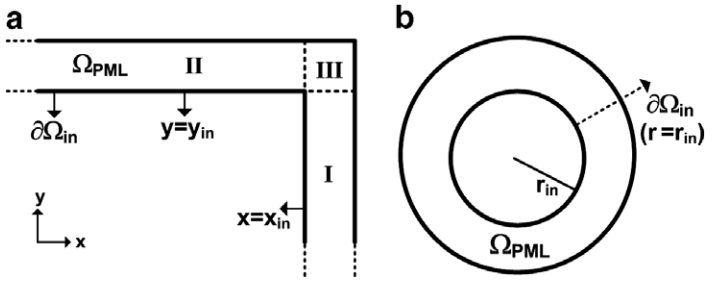

Fig. 3. Classical PML implementations requiring constant coordinate surfaces: (a) cartesian PML; (b) cylindrical PML.

Similarly, if the PML region surrounds a circular spatial domain as shown in Fig. 3b, the classical PML approach in cylindrical coordinates defines the following transformation:

$$\tilde{r} = r + \frac{\alpha}{\mathrm{j}k}(r - r_{\mathrm{in}}). \tag{4}$$

Hence, it should be obvious that the locally-conformal PML method, whose parameter m is 1, reduces to the classical PML approach in such PML regions. However, the classical PML approaches fail if the PML domain encloses an arbitrarily-shaped domain, because inner and outer PML surfaces must be defined on 'constant coordinate surfaces' in these approaches. The locally-conformal PML method remedies this bottleneck and can handle arbitrarily-defined PML surfaces. It is worth to mention that although the outer PML surface is designed as conformal to the inner PML surface as shown in Fig. 1, the geometry of the outer PML surface need not be the same as the inner PML surface. If, for instance, the inner PML surface is designed over a triangular domain, the geometry of the outer PML surface may be elliptical. Thus, the locally-conformal PML method provides a great flexibility in the design of arbitrarily-shaped PML regions.

3. Helmholtz equation in complex space

In the locally-conformal PML approach, the scalar Helmholtz equation is modified through the complex coordinate transformation in Eq. (1). That is, the homogeneous Helmholtz equation in complex space is expressed as

$$\widetilde{\nabla}^2 u^{\mathrm{c}}(\tilde{\vec{r}}) + k^2 u^{\mathrm{c}}(\tilde{\vec{r}}) = 0, \tag{5}$$

where $u^{\mathrm{c}}(\tilde{\vec{r}})$ is the analytic continuation of the unknown function to complex space, and $\widetilde{\nabla}$ is the nabla operator in the complex space and is given by

$$\widetilde{\nabla} = [\overline{\overline{J}}^{-1}]^{\mathrm{T}} \cdot \nabla, \tag{6}$$

where $\overline{\overline{J}}$ is the Jacobian tensor defined as (in 2D Cartesian coordinates)

$$\overline{\overline{J}} = \frac{\partial(\tilde{x}, \tilde{y}, \tilde{z})}{\partial(x, y, z)} = \begin{bmatrix} \partial\tilde{x}/\partial x & \partial\tilde{x}/\partial y & 0 \\ \partial\tilde{y}/\partial x & \partial\tilde{y}/\partial y & 0 \\ 0 & 0 & 1 \end{bmatrix}. \tag{7}$$

When we substitute Eq. (6) into Eq. (5), the partial differential equation in real coordinates is expressed as

$$\left([\overline{\overline{J}}^{-1}]^{\mathrm{T}} \cdot \nabla\right) \cdot \left([\overline{\overline{J}}^{-1}]^{\mathrm{T}} \cdot \nabla u(\vec{r})\right) + k^2 u(\vec{r}) = 0, \tag{8}$$

where $u(\vec{r})$ is the unknown function in real coordinates.

Alternatively, it is known that the coordinate transformation in Eq. (1) changes the original medium into an anisotropic medium ensuring that the Helmholtz equation is still satisfied in the transformed complex space (i.e., Helmholtz equation is form-invariant under space transformations). That is, the free-space Helmholtz equation under coordinate transformation is equivalent to the Helmholtz equation in a material medium with the following tensor constitutive parameters [21]:

$$\bar{\bar{\varepsilon}} = \varepsilon \overline{\overline{\Lambda}}, \tag{9a}$$

$$\bar{\bar{\mu}} = \mu \overline{\overline{\Lambda}}, \tag{9b}$$

where ε and μ are the constitutive parameters of the original isotropic medium ($k = \omega\sqrt{\mu\varepsilon}$ in electromagnetics), and

$$\overline{\overline{\Lambda}} = (\det \overline{\overline{J}})(\overline{\overline{J}}^{\mathrm{T}} \cdot \overline{\overline{J}})^{-1}. \tag{10}$$

For instance, in 2D where $u(\vec{r}) = E(x, y)$, the Helmholtz equation reduces to the following partial differential equation:

$$\nabla \cdot (\overline{\overline{\Lambda}}_{\text{sub}} \nabla u(\vec{r})) + k^2 \Lambda_{33} u(\vec{r}) = 0, \tag{11}$$

where $\overline{\overline{\Lambda}}_{\text{sub}}$ and Λ_{33} are the entries of $\overline{\overline{\Lambda}}$ such that

$$\overline{\overline{\Lambda}} = \begin{bmatrix} \Lambda_{11} & \Lambda_{12} & 0 \\ \Lambda_{21} & \Lambda_{22} & 0 \\ 0 & 0 & \Lambda_{33} \end{bmatrix} \quad \text{and} \quad \overline{\overline{\Lambda}}_{\text{sub}} = \begin{bmatrix} \Lambda_{11} & \Lambda_{12} \\ \Lambda_{21} & \Lambda_{22} \end{bmatrix}. \tag{12}$$

In electromagnetics, the Helmholtz equation in anisotropic medium is expressed in terms of the constitutive parameters of the medium (permittivity and permeability) which are given in Eq. (9). However, the formulation in this section is also applicable for other types of waves, such as acoustical waves, because 2D acoustics and electromagnetics in anisotropic media are exactly equivalent by means of the exact duality between the two sets of parameters as follows [22]:

$$[\rho, \lambda^{-1}] \leftrightarrow [\mu, \varepsilon], \tag{13}$$

where ρ is the fluid mass density and λ is the fluid bulk modulus in acoustics.

An important observation is that the tensor in Eq. (10) is symmetrical, thus, the constitutive parameters in Eq. (9) satisfy the following conditions:

$$\bar{\bar{\varepsilon}} = \bar{\bar{\varepsilon}}^{\text{T}}, \tag{14a}$$

$$\bar{\bar{\mu}} = \bar{\bar{\mu}}^{\text{T}}. \tag{14b}$$

On the basis of these conditions, the anisotropic PML medium is 'reciprocal', implying that the decay characteristics of the waves traveling toward and away from the outer PML boundary must be identical [23]. That is, although the waves decay monotonically when they are transmitted into the PML region, their magnitude is still non-zero when they reach the outer boundary. Then, they are reflected from the outer boundary and they travel in the opposite direction. As a result of reciprocity in the lossy PML medium, the medium characteristics will not be depending on the direction of propagation, and it is guaranteed that the waves reflected from the outer boundary will continue to decay as they approach the inner boundary. An effective PML design is based on the proper choice of the PML parameters yielding negligible field magnitudes after the 'two-way' propagation of the field components, before they enter the inner computational domain.

3.1. Complex space FEM formulation

Although the partial differential equations in Eqs. (8) and (11) in real coordinates can be solved in a FEM program by modifying the original FEM formulation in Ω_{PML}, we prefer to consider the original form of the Helmholtz equation in Eq. (5) in the complex space. In this section, we show that the FEM formulation considering the original form of the Helmholtz equation does not need to be modified in Ω_{PML}. Since the algebraic relations related to the FEM formulation are evaluated in terms of the nodal coordinates, we preserve the original FEM formulation, and we just replace the real coordinates in Ω_{PML} by their complex counterparts calculated via Eq. (1). In other words, the novelty in the following formulations is the implementation of the complex space FEM using complex elements using the original Helmholtz equation.

As a first step, the weak form of the Helmholtz equation in Eq. (5) can be calculated using the method of weighted residuals, and is given in complex space as

$$\int_{\Omega_{\text{PML}}} \tilde{\nabla} u^{\text{c}}(\tilde{\vec{r}}) \cdot \tilde{\nabla} w^{\text{c}} \, \text{d}\Omega - k^2 \int_{\Omega_{\text{PML}}} u^{\text{c}}(\tilde{\vec{r}}) w^{\text{c}} \, \text{d}\Omega = 0, \tag{15}$$

where w^{c} is a scalar weight function in complex space.

In FEM, we solve the weak form of the Helmholtz equation in Eq. (15) by discretizing the computational domain using triangular elements. In the complex coordinate transformation, the triangular elements are mapped to complex triangular elements (i.e., elements with complex node coordinates), as illustrated in Fig. 4a.

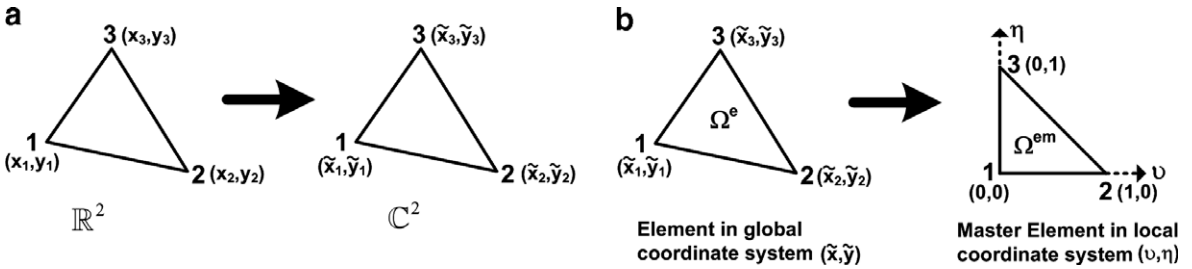

Fig. 4. (a) Mapping of triangular elements to complex triangular elements; (b) isoparametric mapping in FEM formulation.

Within each element, the unknown function is approximated as

$$u^{c,e}(\tilde{\vec{r}}) = \sum_{i=1}^{3} N_i(\tilde{\vec{r}}) u_i^{c,e}, \tag{16}$$

where $u_i^{c,e}$ is the unknown function and $N_i(\tilde{\vec{r}})$ is the shape function for the ith node.

After substituting the expression in Eq. (16) into Eq. (15), we use the Rayleigh–Ritz approach where the weight functions are chosen to be equal to the shape functions (i.e., $w^c = N_i(\tilde{\vec{r}})$). Then, the weak form of the Helmholtz equation becomes

$$\int_{\Omega^e_{PML}} \tilde{\nabla}\left(\sum_{i=1}^{3} N_i(\tilde{\vec{r}}) u_i^{c,e}\right) \cdot \tilde{\nabla} N_j(\tilde{\vec{r}}) \mathrm{d}\Omega - k^2 \int_{\Omega^e_{PML}} \left(\sum_{i=1}^{3} N_i(\tilde{\vec{r}}) u_i^{c,e}\right) N_j(\tilde{\vec{r}}) \mathrm{d}\Omega = 0 \quad (j = 1,2,3). \tag{17}$$

From Eq. (17), we construct a 3×3 local matrix whose ijth entry is given by

$$a_{ij}^e = \int_{\Omega^e_{PML}} [\tilde{\nabla} N_i(\tilde{\vec{r}})] \cdot [\tilde{\nabla} N_j(\tilde{\vec{r}})] \mathrm{d}\Omega - k^2 \int_{\Omega^e_{PML}} N_i(\tilde{\vec{r}}) N_j(\tilde{\vec{r}}) \mathrm{d}\Omega. \tag{18}$$

The integration in Eq. (18) is not performed directly in terms of the global coordinates, but the element is mapped to a master element in local coordinates using the "isoparametric mapping" (see Fig. 4b). In this mapping, both the global coordinates and the unknown function are expressed in terms of the same shape functions.

In each local element, the scalar shape functions are defined as [24]

$$N_1 = 1 - \upsilon - \eta, \tag{19a}$$

$$N_2 = \upsilon, \tag{19b}$$

$$N_3 = \eta. \tag{19c}$$

Using the isoparametric mapping, the coordinate variable variations are expressed in terms of the scalar shape functions and the global node coordinates (in Cartesian coordinates) as follows:

$$\tilde{x} = \sum_{i=1}^{3} \tilde{x}_i N_i(\upsilon, \eta), \tag{20a}$$

$$\tilde{y} = \sum_{i=1}^{3} \tilde{y}_i N_i(\upsilon, \eta). \tag{20b}$$

The unknown function is also expressed as follows:

$$u^{c,e}(\upsilon, \eta) = \sum_{i=1}^{3} N_i(\upsilon, \eta) u_i^{c,e}. \tag{21}$$

Using the expressions in Eq. (20), the Jacobian matrix is calculated as

$$J_{\mathrm{FEM}} = \begin{bmatrix} \partial\tilde{x}/\partial\upsilon & \partial\tilde{y}/\partial\upsilon \\ \partial\tilde{x}/\partial\eta & \partial\tilde{y}/\partial\eta \end{bmatrix} = \begin{bmatrix} \tilde{x}_2 - \tilde{x}_1 & \tilde{y}_2 - \tilde{y}_1 \\ \tilde{x}_3 - \tilde{x}_1 & \tilde{y}_3 - \tilde{y}_1 \end{bmatrix}. \tag{22}$$

The expression in Eq. (22) shows that the entries of the Jacobian matrix are constant, and depend on only the node coordinates.

Then, using Eqs. (19)–(22), the a_{ij}^{e} expression in Eq. (18) becomes

$$a_{ij}^{\mathrm{e}} = \int_{\Omega_{\mathrm{PML}}^{\mathrm{em}}} [\widetilde{\nabla} N_i(\upsilon,\eta)] \cdot [\widetilde{\nabla} N_j(\upsilon,\eta)] \det(J_{\mathrm{FEM}})\, \mathrm{d}\upsilon\, \mathrm{d}\eta - k^2 \int_{\Omega_{\mathrm{PML}}^{\mathrm{em}}} N_i(\upsilon,\eta) N_j(\upsilon,\eta) \det(J_{\mathrm{FEM}})\, \mathrm{d}\upsilon\, \mathrm{d}\eta. \tag{23}$$

In order to evaluate Eq. (23), we need to calculate $\widetilde{\nabla} N_i(\upsilon,\eta)$ expression, which simply depends on the $\widetilde{\nabla}\upsilon$ and $\widetilde{\nabla}\eta$ terms. The components of these terms are entirely determined by the inverse of the Jacobian matrix in Eq. (22), whose entries are given in terms of global node coordinates, as follows:

$$\frac{\partial\upsilon}{\partial\tilde{x}} = [J_{\mathrm{FEM}}^{-1}]_{1,1}, \quad \frac{\partial\upsilon}{\partial\tilde{y}} = [J_{\mathrm{FEM}}^{-1}]_{2,1}, \quad \frac{\partial\eta}{\partial\tilde{x}} = [J_{\mathrm{FEM}}^{-1}]_{1,2}, \quad \frac{\partial\eta}{\partial\tilde{y}} = [J_{\mathrm{FEM}}^{-1}]_{2,2}, \tag{24}$$

where $[J_{\mathrm{FEM}}^{-1}]_{i,j}$ is the ijth entry of the inverse Jacobian matrix.

The formulation in this section shows that the a_{ij}^{e} expression in Eq. (23), which is the ijth entry of the local element matrix, is evaluated in terms of the nodal coordinates. Consequently, the FEM formulation can easily be implemented in the complex space by using the complex-valued node coordinates obtained via the complex coordinate transformation. Although the evaluation of the a_{ij}^{e} expression in terms of the nodal coordinates is given for triangular elements, similar derivations are obviously possible for other types of elements (e.g., quadrilateral).

4. Performance analysis via Monte Carlo simulations

In this section, we report the results of some numerical experiments to test the accuracy of the locally-conformal PML method in two different problems:

(i) Problem of constructing the free-space Green's function for Helmholtz equation with different source positions in a given domain.
(ii) 2D TM_z electromagnetic scattering problem involving a single infinitely-long cylindrical PEC (perfect electric conductor) obstacle with an arbitrary cross-section.

All simulations are performed using our 2D FEM software employing isoparametric triangular elements.

The first problem (see Fig. 5a), which is the construction of the 2D free-space Green's function, is governed by the Helmholtz equation as given below:

$$\nabla^2 u(\vec{r}) + k^2 u(\vec{r}) = -\delta(\vec{r} - \vec{r}_{\mathrm{s}}). \tag{25}$$

The analytical solution of Eq. (25) is given by [25]

$$u^{\mathrm{analytic}}(\vec{r}) = (\mathrm{j}/4) H_0^{(2)}(k|\vec{r} - \vec{r}_{\mathrm{s}}|), \tag{26}$$

where $H_0^{(2)}$ is the Hankel function of the second kind of zeroth order, and $\vec{r}_{\mathrm{s}}$ is an arbitrary location of a point source inside Ω_{PS}. We solve Eq. (25) by converting it into the homogeneous Helmholtz equation with a Dirichlet type boundary condition (BC) as follows:

$$\nabla^2 u(\vec{r}) + k^2 u(\vec{r}) = 0, \tag{27a}$$

$$\text{with BC}: u(\vec{r}) = u^{\mathrm{analytic}}(\vec{r}) \quad \text{on } \partial\Omega_{\mathrm{PS}}. \tag{27b}$$

In PML region Ω_{PML}, Eq. (5), which is actually equivalent to Eq. (27a) in the complex space, is solved simply by interchanging the real coordinates in Ω_{PML} by their complex counterparts calculated by Eq. (1), and preserving the original form of the Helmholtz equation.

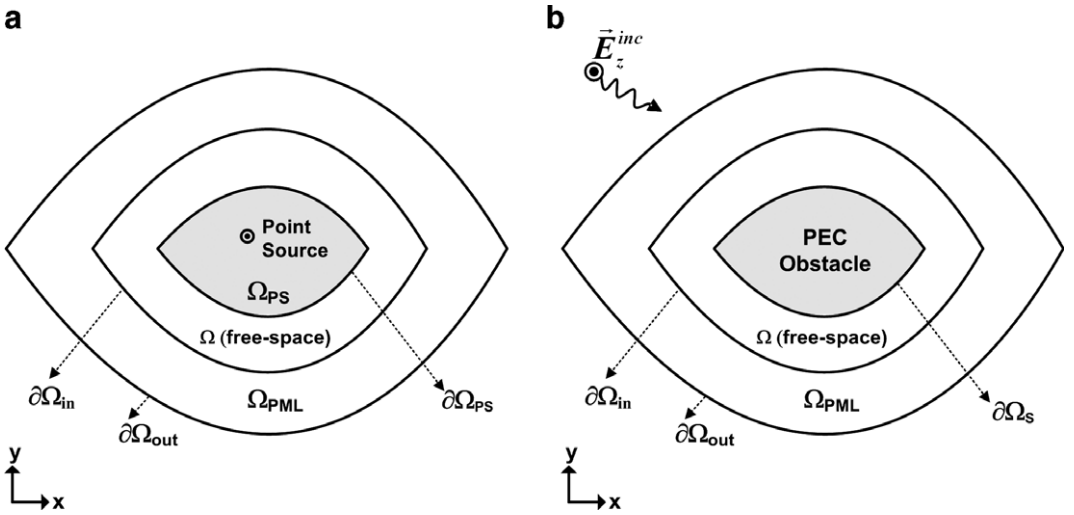

Fig. 5. General models of the two problems under consideration: (a) problem of constructing the 2D free-space Green's function, (b) 2D TM_z electromagnetic scattering problem.

The reason of our choice of Eq. (25) as our model problem in error analysis is closely related to the linearity and space-invariance of problems governed by Helmholtz equation in free space. It is well known that any source function $g(\vec{r})$ (excitation or forcing function) inside a given domain can be represented as a convolution integral with impulses. In this case, Helmholtz equation is expressed as

$$\nabla^2 u(\vec{r}) + k^2 u(\vec{r}) = -\int_{\Omega_g} g(\vec{r}_s)\delta(\vec{r}-\vec{r}_s)\mathrm{d}\vec{r}_s, \tag{28}$$

where $\Omega_g = \mathrm{supp}(g)$. This result implies that the error analysis of the solution of Eq. (25) is critical for *arbitrary* locations of the impulses. Therefore, in the simulation phase of the first problem, we calculate the error statistics by choosing $\vec{r}_s$ as a 'random variable' uniformly distributed in Ω_{PS}. For this purpose, we resort to the 'Monte Carlo' simulation technique in order to get more reliable and robust results, because the accuracy of the method may depend on the position of the point source inside Ω_{PS}. In the Monte Carlo simulation technique, which is a stochastic technique based on the use of random numbers and probability statistics to investigate the problems, we determine randomly '2000 different source positions' inside Ω_{PS}, and we run the FEM program 2000 times using these source positions. Then, for each run, we calculate two different kinds of mean-square error criteria in Ω as follows:

$$E_1 = \frac{\sum_\Omega |u^{\text{calculated}} - u^{\text{analytic}}|^2}{\sum_\Omega |u^{\text{analytic}}|^2}(\times 100) \tag{29}$$

and

$$E_2 = \frac{\sum_\Omega |Lu^{\text{calculated}} - Lu^{\text{analytic}}|^2}{\sum_\Omega |Lu^{\text{analytic}}|^2}(\times 100), \tag{30}$$

where $u^{\text{calculated}}$ and u^{analytic} are the calculated and analytical values in Ω, respectively, and L represents the operator if the original boundary problem can also be modeled as $Lu = f$ in general. The operator L basically represents the resultant global matrix in the FEM formulation. The error in Eq. (30) is also known as 'model error', 'residual error' or 'projection error' in the FEM literature, and accounts for especially the approximation of the solution and the domain (type and size of elements, mesh quality, etc.).

Afterwards, using these 2000 error values calculated by Eqs. (29) and (30) separately, (i) we plot the error scatter contour which shows the error value at each source position, (ii) we plot the error histogram which shows the distribution of the error values, and (iii) we calculate the error statistics (mean, variance, etc.). This process provides a global way for the numerical performance analysis of the locally-conformal PML method in the solution

of the first problem by yielding more *robust* (i.e. independent of source position) analysis results. We expect that the locally-conformal PML method yields acceptable error values irrespective of the source position, implying that an arbitrary source function $g(\vec{r})$ inside Ω_{PS} can be reliably handled by the method.

The second problem (see Fig. 5b), which is the 2D TM_z electromagnetic scattering problem involving a single infinitely-long cylindrical PEC obstacle, is solved by the homogeneous Helmholtz equation with a Dirichlet type boundary condition (BC) for PEC obstacles, as follows:

$$\nabla^2 E_z^{\mathrm{s}} + k^2 E_z^{\mathrm{s}} = 0 \quad \text{in } \Omega, \tag{31a}$$

$$\text{with BC} : E_z^{\mathrm{s}} = -E_z^{\mathrm{inc}} \quad \text{on } \partial\Omega_{\mathrm{S}}, \tag{31b}$$

where E_z^{s} stands for the z-component of the scattered field. In this problem, we measure the performance of the locally-conformal PML method by comparing; (i) the current density ($\vec{J} = a_z J_z$) along the boundary of the obstacle (near-field analysis), and (ii) the RCS profile as a function of the aspect angle (i.e., the angle between the x-axis and the direction of observation), with those calculated by the Method of Moments (MoM) approach. As a remark, the MoM is also a numerical method, introduced by Harrington [26], to solve the integral equations arising in scattering and radiation problems in electromagnetics. In the MoM, the boundary of the cylindrical obstacle ($\partial\Omega_{\mathrm{S}}$) is decomposed into a finite number of line segments, and the unknown current density is approximated on these segments using locally-defined basis functions. After solving for the current density over this boundary, the scattered field is calculated in terms of the radiation integrals.

The scattering problem expressed in Eq. (31) is actually equivalent to the following Helmholtz equation:

$$\nabla^2 E_z^{\mathrm{s}} + k^2 E_z^{\mathrm{s}} = \mathrm{j}\omega\mu \oint_{\partial\Omega_{\mathrm{s}}} J_z(\vec{r}\,')\delta(\vec{r} - \vec{r}\,')\mathrm{d}\vec{r}\,'. \tag{32}$$

It is evident that the sources of E_z^{s} are located on $\partial\Omega_{\mathrm{s}}$. Thus, the scattering problem may be interpreted as the problem given in Eq. (28) where the source function $g(\vec{r})$ is restricted on the boundary of the domain $\partial\Omega_{\mathrm{PS}}$. In this way, the scattering problem provides an opportunity to consider sources equidistant from the PML interface.

By analogy to the scattering problem, the Monte Carlo simulation of the first problem (viz., Green's function) may also be performed by restricting the random variable $\vec{r}_{\mathrm{s}}$ on a boundary $\partial\Omega_{\mathrm{MC}}$ which is located equidistantly and very close to $\partial\Omega_{\mathrm{PS}}$ within the domain Ω_{PS}. This case (as well as the scattering problem case) may be regarded as the 'worst case' where the distance between each source point and the PML interface in the vicinity of the source point is smallest. Similar to the above-mentioned phases of the Monte Carlo simulation, we present the error statistics by choosing 2000 different source positions along the boundary $\partial\Omega_{\mathrm{MC}}$.

In the following, the three sections are categorized with respect to the mesh structure of the computational domain, because, in each section, the same mesh structure is employed in the solution of both problems, but with different interpretations. That is, in the first problem, the mesh of the whole computational domain Ω_{C}, which is of the cylindrical shell geometry, is assumed to be constructed conformally over a region Ω_{PS} having a point source inside (see Fig. 5a). However, in the second problem, the mesh of Ω_{C} is assumed to be constructed conformally over a PEC obstacle (see Fig. 5b). Therefore, in each section, we first report the Monte Carlo simulation results of the first problem (i.e., Green's function) for a given geometry. Then, we demonstrate the results of the second problem (i.e., scattering problem) for the same geometry.

In the experiments below, we consider some 'computationally difficult' geometries in order to illustrate the performance of the locally-conformal PML approach in handling these cases. The common parameters in all experiments are chosen as (unless otherwise stated): k is 20π (i.e., the wavelength λ is 0.1 m), m is 3, and α is chosen in the range between $7k$ and $10k$. In addition, the PML thickness is approximately set to $\lambda/4$, and the edge size of each triangular element in the mesh is approximately adjusted to $\lambda/60$. In all experiments, almost the same approach is followed to present the results (i.e., the order and the format of the plots, etc.) for the sake of uniformity.

4.1. Conformal PML over an elliptical domain

In the first example, the free-space region Ω is designed conformally over an elliptical domain, and the PML region Ω_{PML} is constructed as conformal to Ω. The semi-major axis of the inner boundary of the elliptical shell

($\partial\Omega_S$ or $\partial\Omega_{PS}$) is 2λ, and the axial ratio is set to 2. All distance parameters (such as the PML thickness and the distance between the sources and $\partial\Omega_{PS}$) can be visualized in Figs. 6 and 7.

In the realization of the Monte Carlo technique for the first problem assuming that the random variable (i.e., source position $\vec{r}_s$) is uniformly distributed in Ω_{PS}, we plot the error scatter plot in Fig. 6a, and the error histogram in Fig. 6b for E_1. Similarly, we plot the error scatter plot in Fig. 6c, and the error histogram in Fig. 6d for E_2. We also show some statistical error values (i.e., mean, variance, etc.) on the plots in Fig. 6b and d.

As a special case of the previous simulation, we assume that the random variable is restricted on a boundary $\partial\Omega_{MC}$ which is located equidistantly and very close ($\sim\lambda/10$) to $\partial\Omega_{PS}$ within the domain Ω_{PS}. Then, we plot the error scatter plots in Fig. 7a and b for E_1 and E_2, respectively, together with the error statistics.

For the second problem which is the electromagnetic scattering problem, we plot the magnitude of the current density along the boundary of the elliptical obstacle and the RCS profile in Fig. 8a and b, respectively. We assume that the angle of incidence of the plane wave is 180° (with respect to the x-axis).

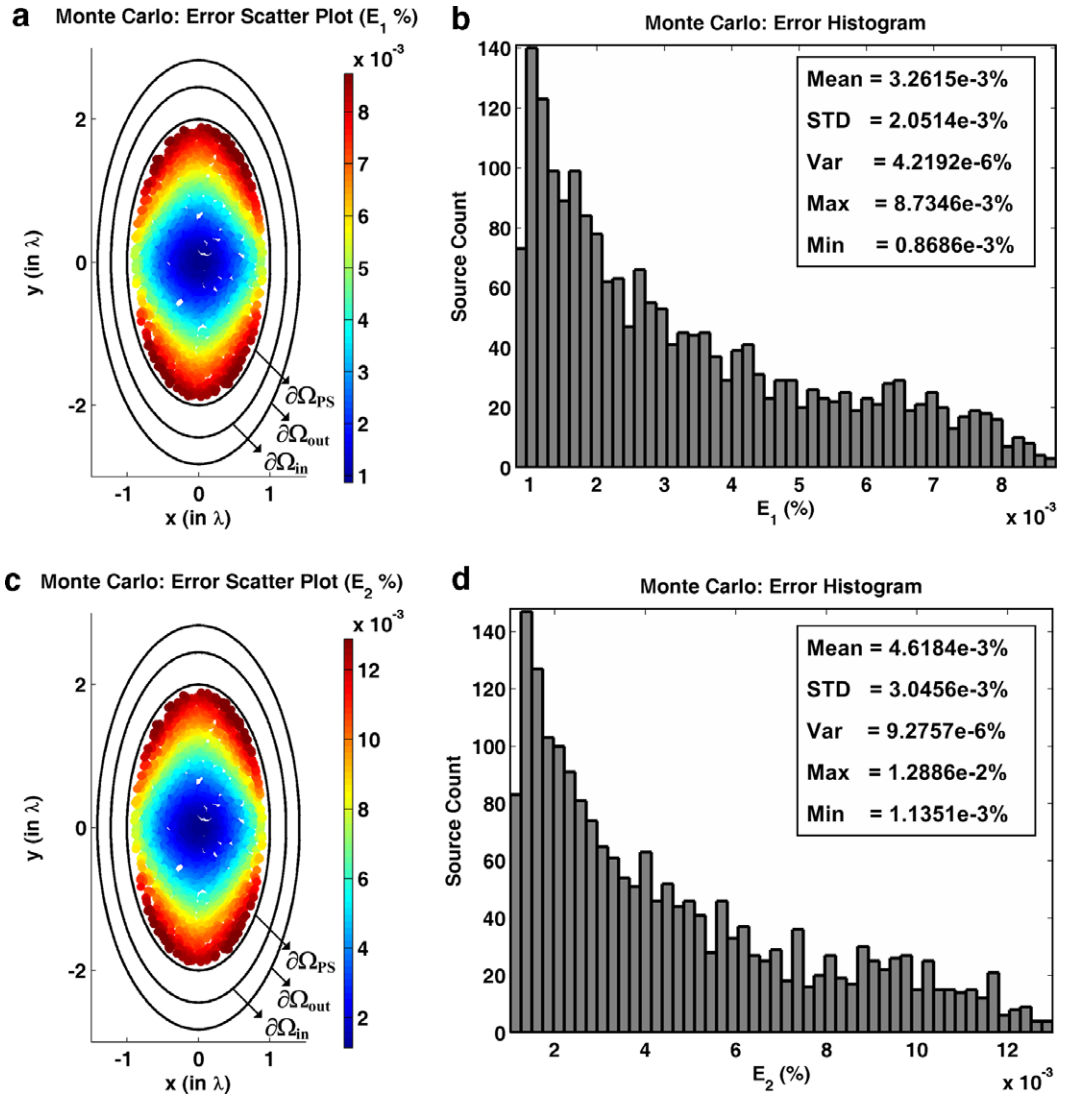

Fig. 6. Error analysis in the Monte Carlo simulation of the free-space Green's function in elliptical domain: (a) error scatter plot for E_1; (b) error histogram and statistics for E_1; (c) error scatter plot for E_2; (d) error histogram and statistics for E_2.

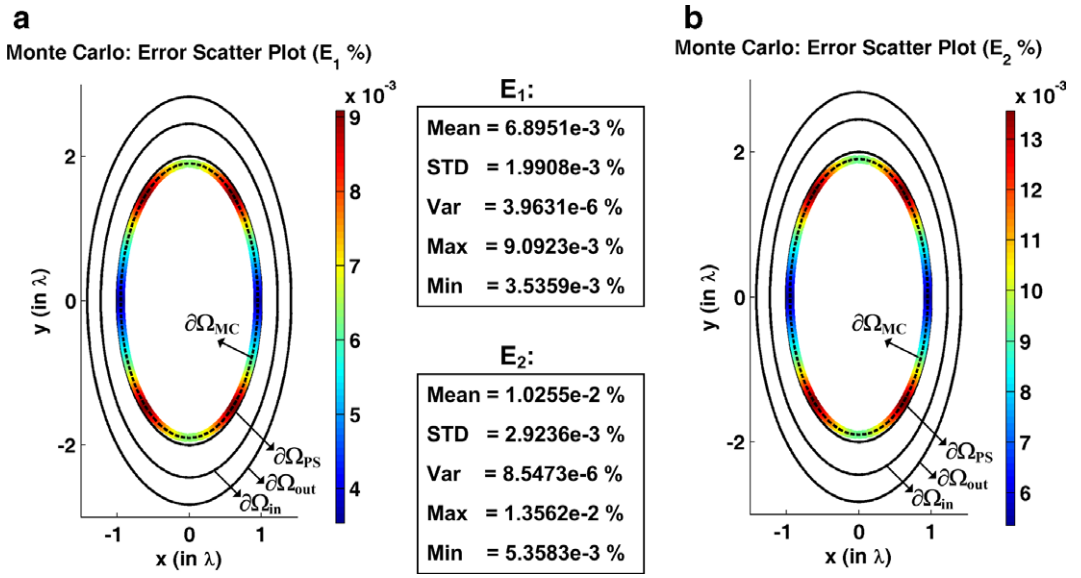

Fig. 7. Monte Carlo simulation restricted to $\partial\Omega_{MC}$ which is located close to $\partial\Omega_{PS}$ [elliptical domain]: (a) error scatter plot for E_1; (b) error scatter plot for E_2.

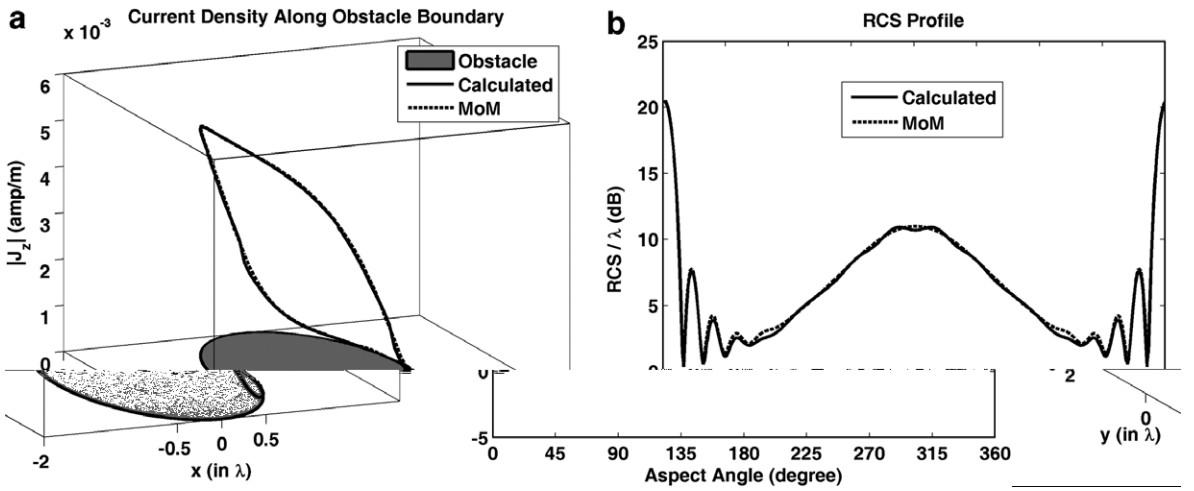

Fig. 8. Scattering problem involving infinitely-long elliptical PEC cylinder: (a) magnitude of current density along the obstacle boundary; (b) RCS profile.

4.2. Conformal PML over a triangular_plus_halfcircular domain

In this example, a conformal PML is designed over a triangular_plus_halfcircular domain. The radius of the inner boundary of the shell ($\partial\Omega_S$ or $\partial\Omega_{PS}$) is 1.6λ, and the triangle (nose) angle is 90°. All distance parameters can be visualized in Figs. 9 and 10.

For the Monte Carlo simulation of the first problem assuming that the random variable is uniformly distributed in Ω_{PS}, we plot the error scatter plots and error histograms in Fig. 9 for both E_1 and E_2. Then, assuming that the random variable is restricted on $\partial\Omega_{MC}$, we again perform the Monte Carlo simulation and we plot the error scatter plots in Fig. 10.

In addition, in order to better visualize the wave behavior inside the PML region, we place a 'single' point source close to the right corner of the boundary $\partial\Omega_{PS}$. Then, we plot the magnitude and phase of the Green's

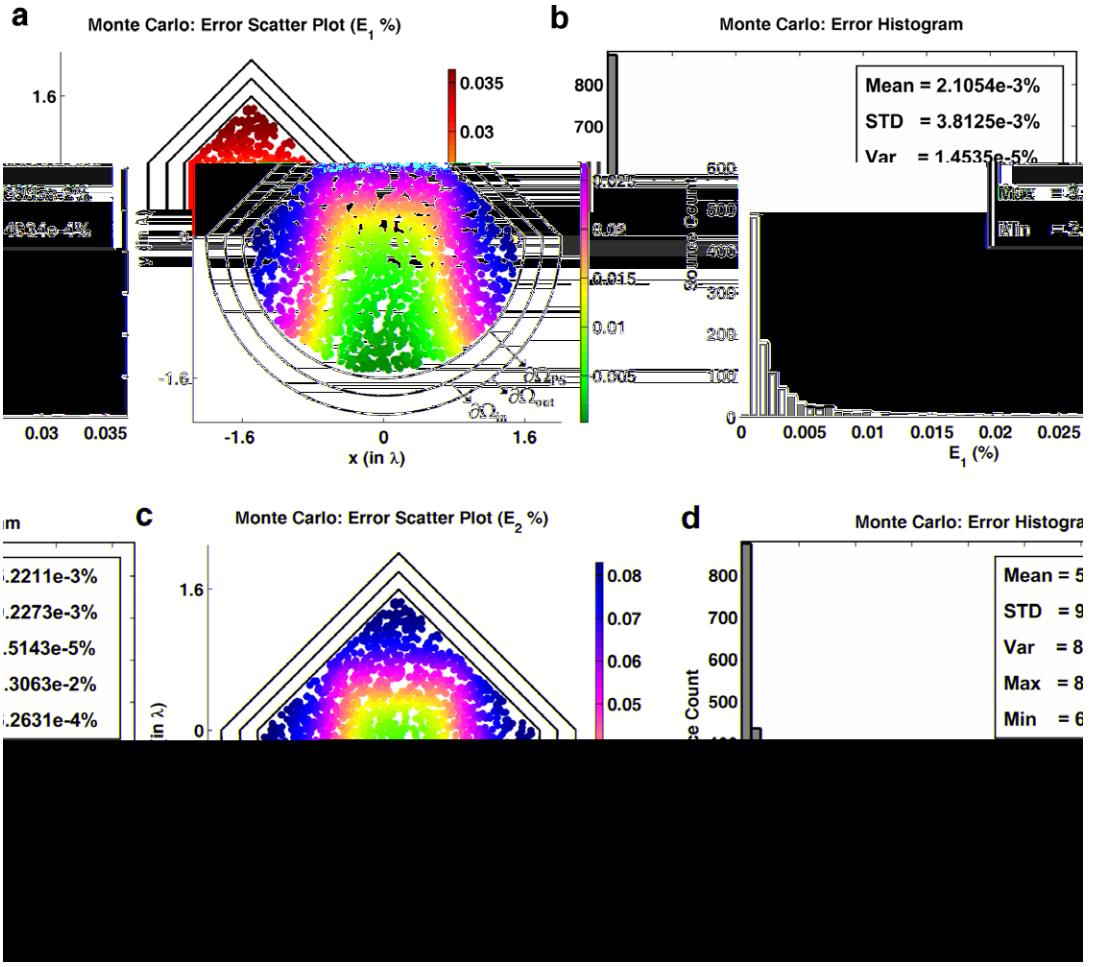

Fig. 9. Error analysis in the Monte Carlo simulation of the free-space Green's function in triangular_plus_halfcircular domain: (a) error scatter plot for E_1; (b) error histogram and statistics for E_1; (c) error scatter plot for E_2; (d) error histogram and statistics for E_2.

function along the x-axis in Fig. 11. The magnitude plot proves that the magnitude of the function decays smoothly inside the PML region, regardless of the distance between the source position and the PML interface.

For the second problem, the magnitude of the current density along the boundary of the obstacle and the RCS profile are plotted in Fig. 12a and b, respectively, for the infinitely-long PEC cylindrical obstacle. The angle of incidence of the plane wave is set to 90° (nose-on incidence).

4.2.1. Analysis of the PML parameters

In this section, we demonstrate the effect of the PML parameters (d_{PML}, α and m) on the performance of the PML by running several Monte Carlo simulations using the same source positions in Fig. 9 in a triangular_plus_halfcircular domain. Since this particular geometry includes variations in interface curvatures, as well as curvature discontinuities, it is taken as a test problem to examine the dependence of PML performance on the design parameters of the PML. First, we tabulate the mean values of E_1 and E_2 as a function of the PML thickness d_{PML} in Table 1, by keeping the values of α and m fixed ($\alpha = 10k$ and $m = 3$) in all cases. As shown in this table, the error decreases as the PML thickness increases, because the reflections from the outer boundary $\partial\Omega_{\mathrm{out}}$ decrease owing to the increase in d_{PML}. At the extreme case, there is no reflected wave if the PML region extends to infinity. If d_{PML} is 'large' enough, then the error values E_1 and E_2, which are calculated with respect to the analytical results, include only the finite element discretization errors, but not the

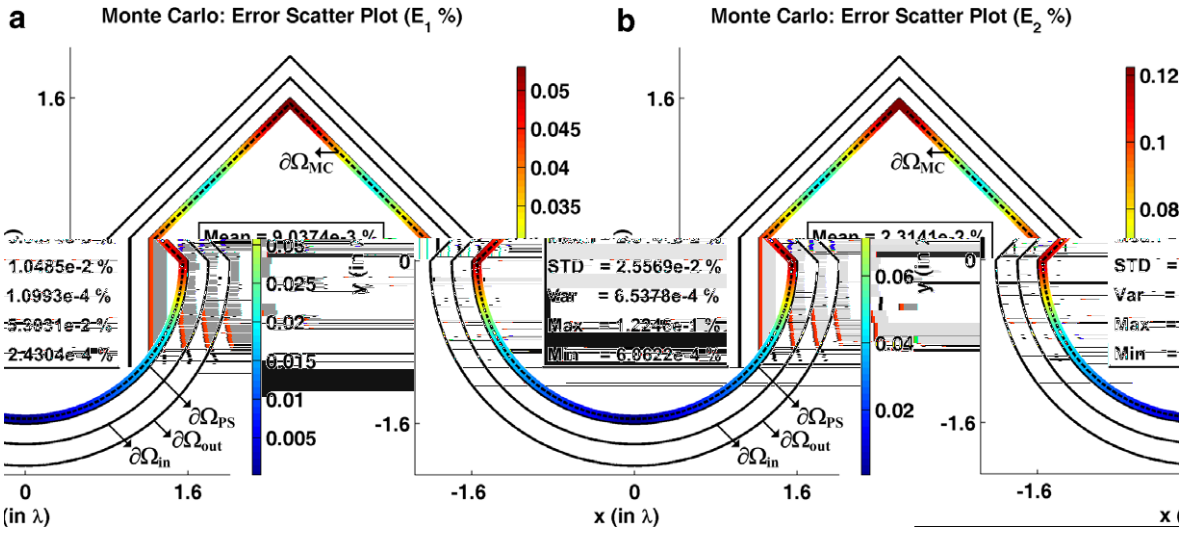

Fig. 10. Monte Carlo simulation restricted to $\partial\Omega_{MC}$ which is located close to $\partial\Omega_{PS}$ [triangular_plus_halfcircular domain]: (a) error scatter plot for E_1; (b) error scatter plot for E_2.

reflection errors. In Table 1, the decay in E_1 and E_2 is fast up to $d_{PML} = \lambda$, and is almost negligible after this distance. Therefore, we can assert that the reflection error for $d_{PML} = 2\lambda$ is almost zero, and the small error values of E_1 and E_2 in this case are due to the discretization errors. In order to eliminate the error contribution due to discretization, we may set the case where $d_{PML} = 2\lambda$ to be the "reference" case, and define a new error criterion as follows:

$$E_3 = \frac{\sum_{\Omega}|u^{\text{calculated}} - u^{\text{reference}}|^2}{\sum_{\Omega}|u^{\text{reference}}|^2}(\times 100), \tag{33}$$

where $u^{\text{reference}}$ is the reference field values in Ω calculated by setting $d_{PML}=2\lambda$, and $u^{\text{calculated}}$ is the calculated field values in Ω for an arbitrary value of $d_{PML} < 2\lambda$. Then, we tabulate E_3 values in Table 1. We observe that E_3 values are less than E_1 values due to the elimination of discretization errors. In conformity to the above discussion, the error decays as d_{PML} increases. However, this table reveals that the error values can be considered at an acceptable level even for electrically thin PML regions.

Second, we calculate the mean values of E_1 and E_2 as a function of the parameter α for two different d_{PML} values ($d_{PML} = \lambda/4$ and $d_{PML} = \lambda/8$), by keeping the value of m fixed ($m = 3$). Then, we plot the error values using a logarithmic scale in Fig. 13a and b for $d_{PML} = \lambda/4$ and $d_{PML} = \lambda/8$, respectively. We can conclude from these plots that the value of α should be large enough to attain a negligible field value on the outer PML boundary. However, if a much larger value of α is chosen, the results start to deteriorate because the coordinate transformation in Eq. (1) yields deformations in the nodal coordinates due to very large imaginary parts. In other words, the shape of the mesh elements in complex space becomes poor in quality due to the improperly transformed coordinates. This may cause ill-conditioning in the global matrix equation, yielding inaccurate analysis results. Hence, the optimal value of α should be essentially determined for a successful PML realization. However, the choice of α is not generally a difficult task because it may be chosen over a wide interval, as shown in Fig. 13, depending on the PML thickness. Practically, $5k \leqslant \alpha \leqslant 15k$ yields reliable results for a PML thickness between $\lambda/4$ and $\lambda/2$. As the PML thickness decreases, a relatively larger value of α can be employed to achieve a more successful PML design.

Finally, we tabulate the mean values of E_1 and E_2 as a function of the parameter m in Table 2, by keeping the values of α and d_{PML} fixed ($\alpha = 10k$ and $d_{PML} = \lambda/4$) in all cases. We conclude from this table that m can typically be chosen as 2 or 3 in order to achieve a smooth decay inside the PML region, because the value of m determines the decay profile (or decay rate) inside the PML region. If m increases, the waves are forced to decay very slowly in regions close to the inner PML boundary $\partial\Omega_{in}$, and the decay rate increases sharply close

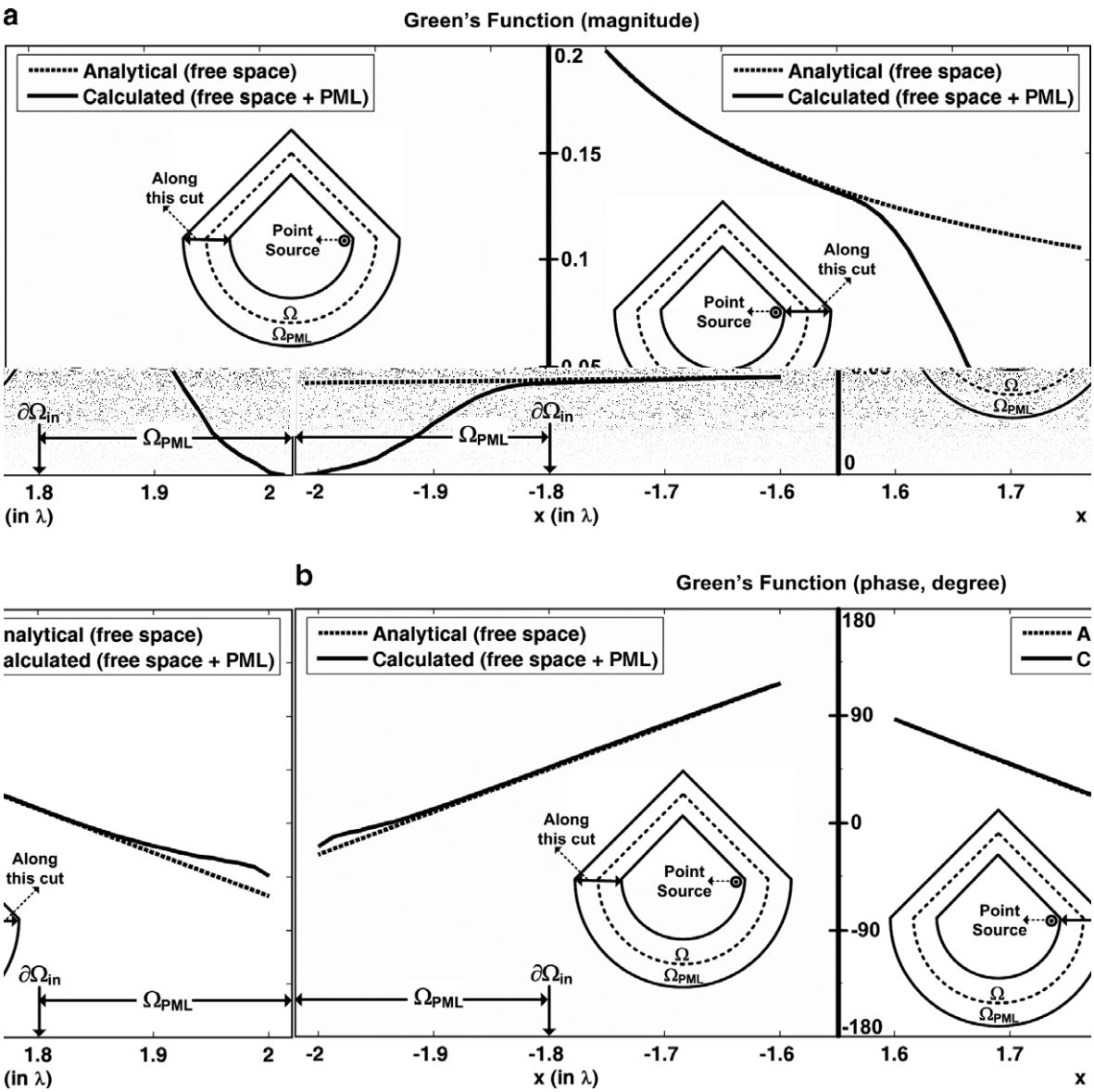

Fig. 11. Green's function along the x-axis in triangular_plus_halfcircular domain [a single point source is located close to the right corner of the domain]: (a) magnitude; (b) phase.

to the outer PML boundary $\partial\Omega_{\text{out}}$, due to the behavior of the exponential function in Eq. (2), which exhibits slow growth at points close to $\partial\Omega_{\text{in}}$ and a much faster growth rate close to $\partial\Omega_{\text{out}}$.

4.3. Conformal PML over a quadrilateral domain

The next example is a conformal PML designed over a quadrilateral domain. The vertex coordinates of the inner boundary of the shell ($\partial\Omega_{\text{S}}$ or $\partial\Omega_{\text{PS}}$) are (in terms of λ): vertex 1: $(-2, 2)$, vertex 2: $(-4, -2)$, vertex 3: $(4, -4)$ and vertex 4: $(10, 4)$, in Cartesian coordinates.

For the Monte Carlo simulation of the first problem assuming that the random variable is uniformly distributed in Ω_{PS}, we plot the error scatter plots and error histograms in Fig. 14 for E_1 and E_2. For the Monte Carlo simulation with random variable restricted on $\partial\Omega_{\text{MC}}$, we plot the error scatter plots in Fig. 15.

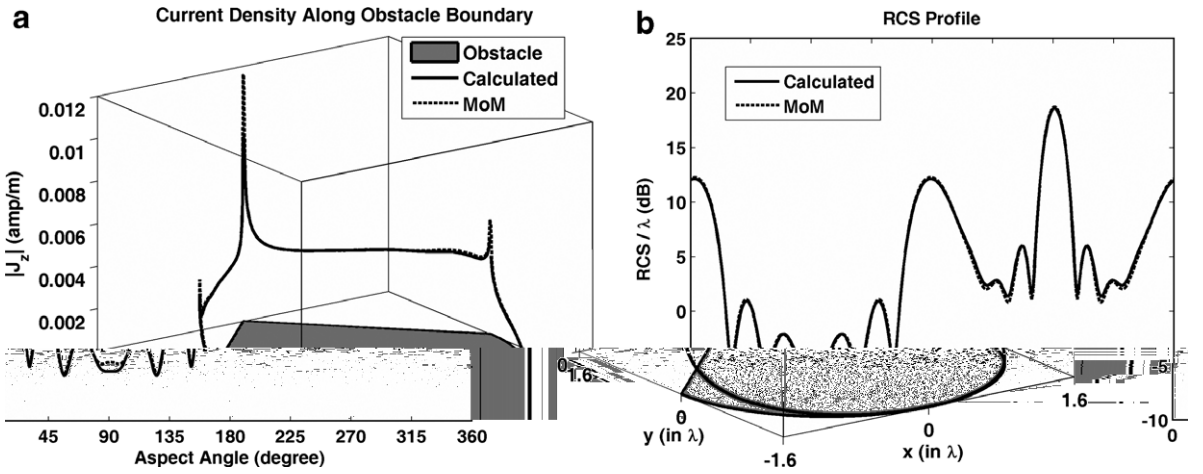

Fig. 12. Scattering problem involving infinitely-long triangular_plus_halfcircular PEC cylinder: (a) magnitude of current density along the obstacle boundary; (b) RCS profile.

Table 1
Mean error values for different values of d_{PML} ($\alpha = 10k$ and $m = 3$)

d_{PML}	E_1 (%)	E_2 (%)	E_3 (%)
$\lambda/16$	7.1034e−1	1.6775	7.0760e−1
$\lambda/8$	6.0180e−2	1.5497e−1	5.9421e−2
$\lambda/4$	2.1054e−3	5.2211e−3	2.0205e−3
$\lambda/2$	1.3984e−4	2.6982e−4	4.0109e−5
$3\lambda/4$	8.3918e−5	1.7085e−4	8.8977e−6
λ	6.7296e−5	1.4204e−4	2.6532e−6
2λ	5.5044e−5	1.2044e−4	(Reference)

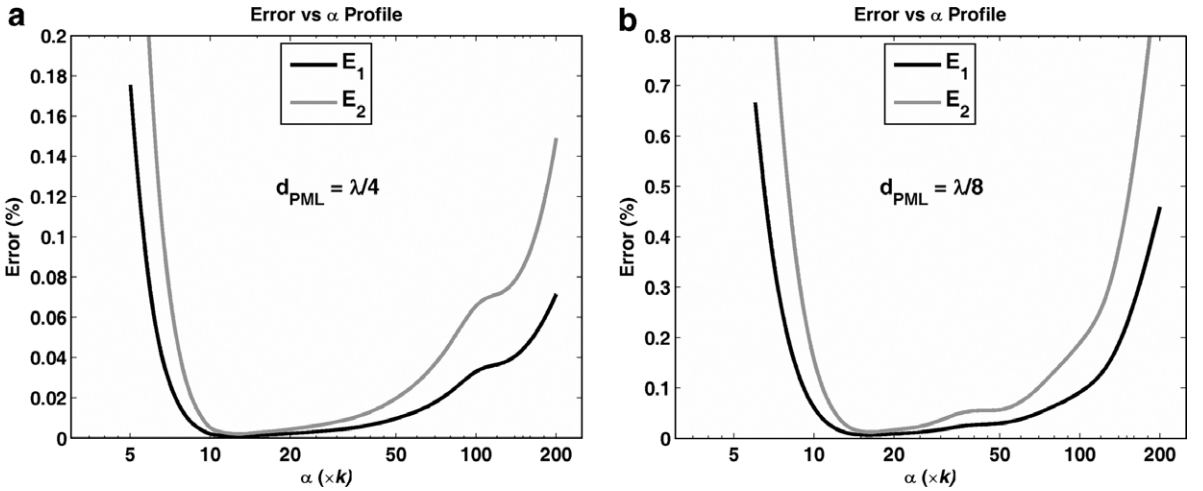

Fig. 13. Error variations as a function of α for $m = 3$ in triangular_plus_halfcircular domain (log scale): (a) $d_{\mathrm{PML}} = \lambda/4$, (b) $d_{\mathrm{PML}} = \lambda/8$.

For the second problem, the magnitude of the current density along the boundary of the obstacle and the RCS profile are plotted in Fig. 16a and b, respectively, for the infinitely-long PEC cylindrical obstacle. The angle of incidence of the plane wave is set to 180°.

Table 2
Mean error values for different values of m ($d_{\mathrm{PML}} = \lambda/4$ and $\alpha = 10k$)

m	E_1 (%)	E_2 (%)
1	6.1829e−1	1.6624
2	9.9935e−4	1.7193e−3
3	2.1054e−3	5.2211e−3
4	1.6573e−2	4.2746e−2
5	6.2999e−2	1.5905e−1

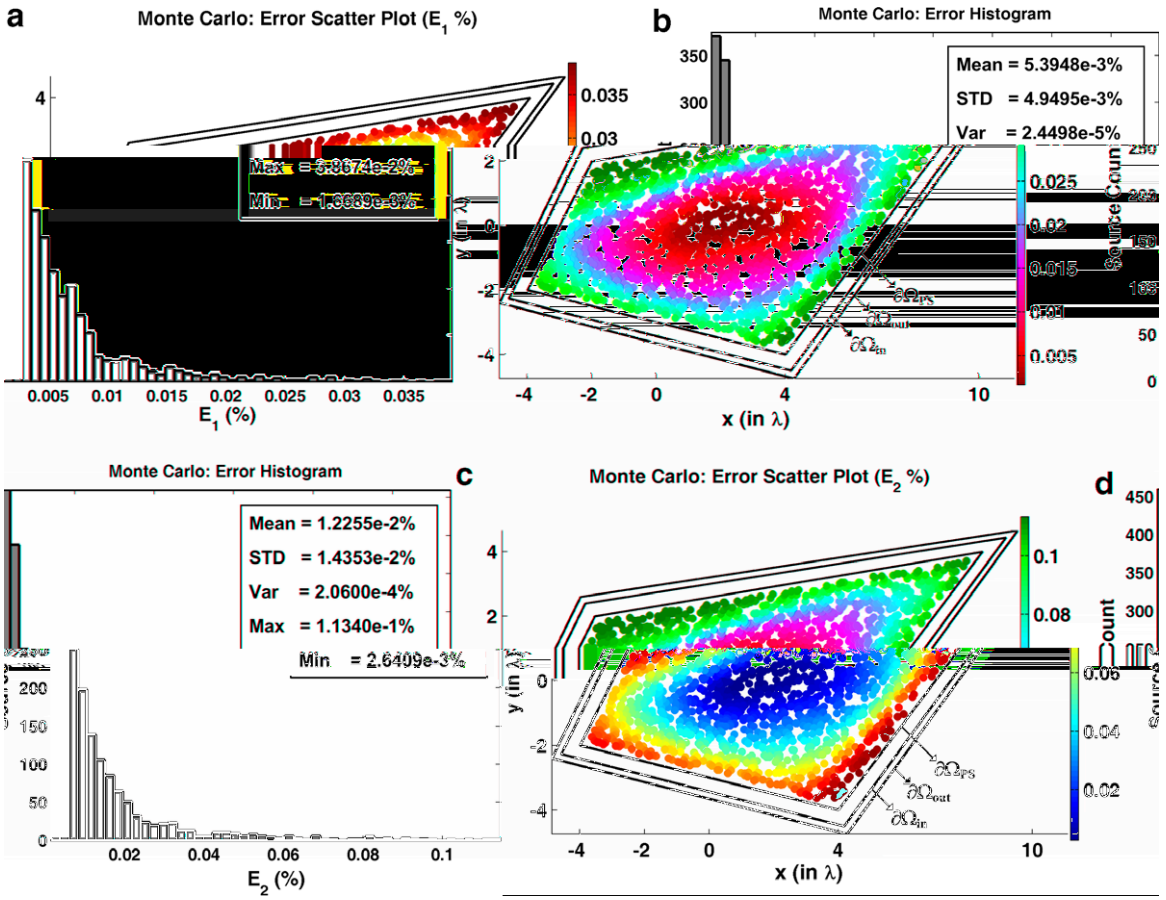

Fig. 14. Error analysis in the Monte Carlo simulation of the free-space Green's function in quadrilateral domain: (a) error scatter plot for E_1; (b) error histogram and statistics for E_1; (c) error scatter plot for E_2, (d) error histogram and statistics for E_2.

The numerical experiments in this section demonstrate that the results calculated by the locally-conformal PML method are sufficiently close to the reference results, and these examples prove that the locally-conformal PML is an efficient absorber for the FEM mesh truncation having challenging geometries. We also conclude from the error scatter plots that the error values (E_1 or E_2) are at an acceptable level irrespective of the position of the point source. However, the error values get slightly higher close to the boundary of the region Ω_{PS}, especially at the sharper edges of some geometries (such as quadrilateral). This observation is not surprising, since the solution of Helmholtz equation in Eq. (25) becomes singular at the source location. In addition, it is known that the sharp edges may have some effect on the accuracy of the results, compared to the smooth sections of the geometry. In any case, due to the acceptable levels of error values at arbitrary source positions, we can assert that any source function inside the domain can be reliably analyzed by the locally-conformal PML method. Moreover, the numerical experiments show that the PML parameters (d_{PML}, α and m) can be determined

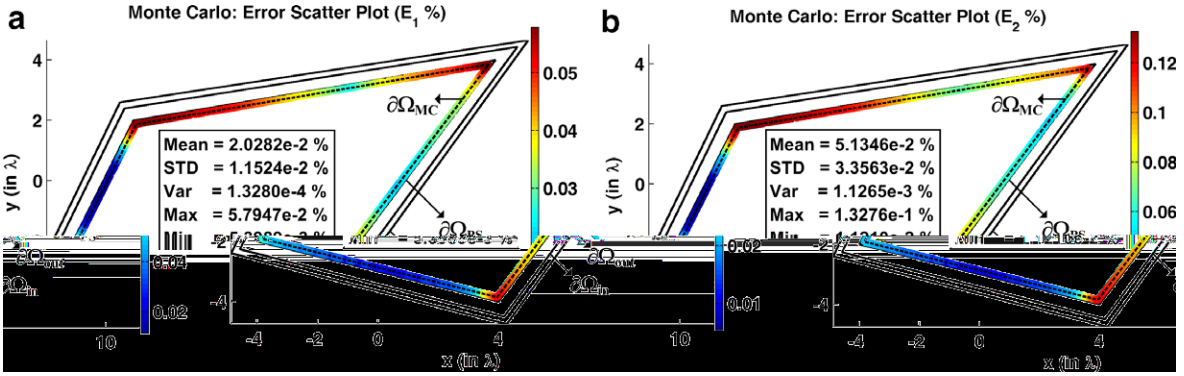

Fig. 15. Monte Carlo simulation restricted to $\partial\Omega_{MC}$ which is located close to $\partial\Omega_{PS}$ [quadrilateral domain]: (a) error scatter plot for E_1; (b) error scatter plot for E_2.

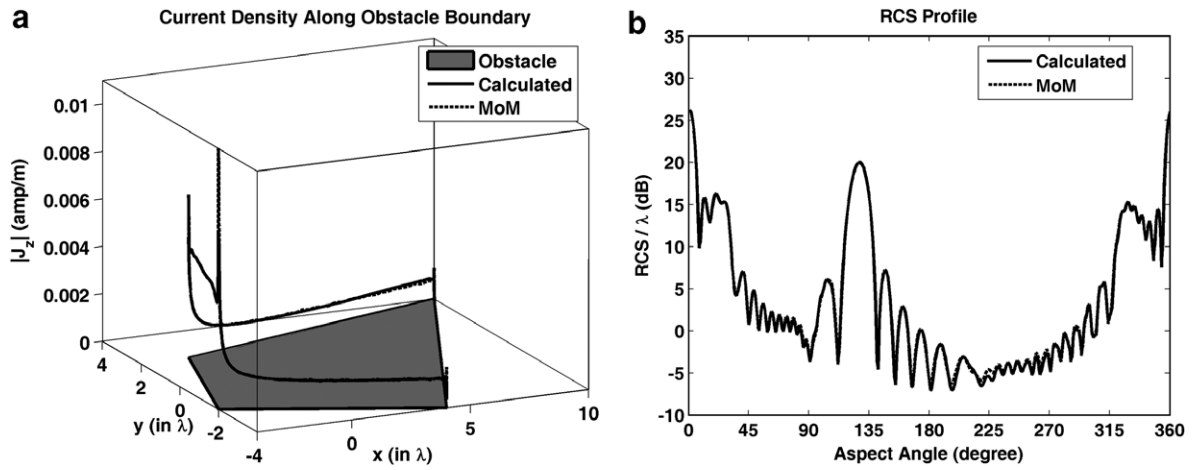

Fig. 16. Scattering problem involving infinitely-long quadrilateral PEC cylinder: (a) magnitude of current density along the obstacle boundary; (b) RCS profile.

properly in a straightforward manner in order to get a monotonic decay inside the PML region, and even thin PML regions (with thickness in the order of a fraction of a wavelength) can provide reliable results.

5. Conclusions

In this paper, we have explored the numerical performance of the locally-conformal PML method for the solution of 2D scalar Helmholtz equation by utilizing the Monte Carlo simulation technique and the FEM in different configurations. We have demonstrated that the implementation of this method in a FEM code is straightforward, and it makes possible the design of conformal PMLs for computational domains having arbitrary convex geometries. After interchanging the real node coordinates inside the PML region with the complex counterparts obtained by the complex coordinate transformation, a successful PML design can be achieved without altering the original FEM formulation.

Appendix

In this section, we demonstrate how the coordinate transformation in Eq. (1) guarantees the fulfillment of the three conditions enumerated by (i, ii, iii) in Section 2 for a scalar wave. Let us first consider a typical plane wave impinging on the PML/free-space interface ($\partial\Omega_{in}$) as follows:

$$u(\vec{r}) = \exp[-\mathrm{j}k\hat{a}_k \cdot \vec{r}], \tag{A.1}$$

where $\hat{a}_k$ is the unit vector representing the direction of incidence. The wave in Eq. (A.1) may represent the z-component of the electric field E_z in TM_z case, or of the magnetic field H_z in TE_z case in electromagnetic wave propagation applications. It is worth mentioning that any outgoing wave can be locally represented as a superposition of plane waves (i.e., local plane wave spectrum). Hence, the wave representation in Eq. (A.1) can be conveniently employed as a sufficiently general case.

Under the coordinate transformation $T : \Omega_{\mathrm{PML}} \to \Gamma$ defined by $\tilde{\vec{r}} = T(\vec{r})$ in Eq. (1) in Section 2, we obtain the wave $\tilde{u}(\tilde{\vec{r}})$ in Ω_{PML} (i.e., analytic continuation of $u(\vec{r})$ to complex space) as follows:

$$\tilde{u}(\tilde{\vec{r}}) = \exp[-\mathrm{j}k\hat{a}_k \cdot \tilde{\vec{r}}]. \tag{A.2}$$

This result is a consequence of the form-invariance property of the Maxwell's equations [21], as well as of the scalar Helmholtz equation which can be derived from (2D) Maxwell's equations, under coordinate transformations, as explained in Section 3. Then, using the transformation in Eq. (1), the expression in Eq. (A.2) can be written explicitly as

$$\begin{aligned}\tilde{u}(\tilde{\vec{r}}) &= \exp[-\mathrm{j}k\hat{a}_k \cdot \vec{r}] \cdot \exp[-f(\xi)\hat{a}_k \cdot \hat{n}(P, P_0)] \\ &= u(\vec{r}) \cdot \exp[-f(\xi)\hat{a}_k \cdot \hat{n}(P, P_0)].\end{aligned} \tag{A.3}$$

It is evident from Eq. (2) that $f(\xi = 0) = 0$ for $\vec{r} \in \partial\Omega_{\mathrm{in}}$. Thus, $u(\vec{r}) = \tilde{u}(\tilde{\vec{r}})$ on the PML/free-space interface. This result guarantees the continuity of the transmitted wave at the interface $\partial\Omega_{\mathrm{in}}$, and thus satisfies the condition (i).

As mentioned in Section 2, in $f(\xi)$, ξ represents the "distance" from the PML point to the interface $\partial\Omega_{\mathrm{in}}$. It should also be noted that the definition of ξ is independent of the curvature of the interface as explained in Section 2. Since $f(\xi)$ is obviously a positive and monotonically increasing function of ξ, the expression $\exp[-f(\xi)\hat{a}_k \cdot \hat{n}(P, P_0)]$ becomes a monotonically decreasing function of ξ (we note that $\hat{a}_k \cdot \hat{n}(P, P_0) > 0$ to be in conformity with the assumption that the original wave is outgoing). This result ensures the monotonic decay of the wave inside the PML region, hence satisfies the condition (ii).

As mentioned in Section 3, although the waves decay monotonically inside the PML region, their magnitude may still be non-zero when they reach the outer boundary $\partial\Omega_{\mathrm{out}}$ and they may be reflected from this boundary. If the PML region has infinite extent, a reflected field is not observed due to the absence of an outer boundary. However, the PML region must be truncated by an outer boundary to render the computational domain finite. In order to satisfy the condition (iii) such that the magnitude of the transmitted wave must attain a negligible value on $\partial\Omega_{\mathrm{out}}$ (i.e., $\exp[-f(\xi)\hat{a}_k \cdot \hat{n}(P, P_0)]|_{\mathrm{on}\ \partial\Omega_{\mathrm{out}}} \approx 0$), the PML parameters ($\mathrm{d}_{\mathrm{PML}}$, α and m) must be selected properly, as demonstrated numerically in Section 4.2.1.

References

[1] J.P. Berenger, A perfectly matched layer for the absorption of electromagnetic waves, J. Comput. Phys. 114 (1994) 185–200.
[2] J.C. Weihl, R. Mittra, Efficient implementation of Berenger's perfectly matched layer (PML) for finite-difference-time-domain mesh truncation, IEEE Microwave Guided Wave Lett. 6 (1996) 94–96.
[3] S.D. Gedney, Anisotropic perfectly matched layer-absorbing medium for the truncation of FDTD lattices, IEEE Trans. Antennas Propag. 44 (1996) 1630–1639.
[4] M.S. Tong, Y.C. Chen, M. Kuzuoglu, R. Mittra, A new anisotropic perfectly matched layer medium for mesh truncation in finite difference time domain analysis, Int. J. Electron. 9 (1999) 1085–1091.
[5] Z.S. Sacks, D.M. Kingsland, R. Lee, J.F. Lee, A perfectly matched anisotropic absorber for use as an absorbing boundary condition, IEEE Trans. Antennas Propag. 43 (1995) 1460–1463.
[6] M. Kuzuoglu, R. Mittra, Investigation of nonplanar perfectly matched absorbers for finite element mesh truncation, IEEE Trans. Antennas Propag. 45 (1997) 474–486.
[7] M. Kuzuoglu, R. Mittra, Mesh truncation by perfectly matched anisotropic absorbers in the finite element method, Microwave Opt. Technol. Lett. 12 (1996) 136–140.
[8] Q. Qi, T.L. Geers, Evaluation of the perfectly matched layer for computational acoustics, J. Comput. Phys. 139 (1998) 166–183.
[9] Q. Liu, J. Tao, The perfectly matched layer for acoustic waves in absorptive media, J. Acoust. Soc. Am. 102 (1997) 2072–2082.
[10] U. Basu, A.K. Chopra, Perfectly matched layers for time-harmonic elastodynamics of unbounded domains: theory and finite-element implementation, Comput. Methods Appl. Mech. Eng. 192 (2003) 1337–1375.

[11] W.C. Chew, Q. Liu, Perfectly matched layers for elastodynamics: a new absorbing boundary condition, J. Comput. Acoust. 4 (1996) 341–359.
[12] J.S. Hesthaven, On the analysis and construction of perfectly matched layers for the linearized Euler equations, J. Comput. Phys. 142 (1998) 129–147.
[13] G.H. Fang, A perfectly matched layer absorbing boundary condition for linearized Euler equations with a non-uniform mean flow, J. Comput. Phys. 208 (2005) 469–492.
[14] T.L. Kosmanis, T.V. Yioultsis, T.D. Tsiboukis, Perfectly matched anisotropic layer for the numerical analysis of unbounded eddy-current problems, IEEE Trans. Magn. 35 (1999) 4452–4458.
[15] Y.Q. Zeng, J.Q. He, Q.H. Liu, The application of the perfectly matched layer in numerical modeling of wave propagation in poroelastic media, Geophysics 66 (2001) 1258–1266.
[16] W.C. Chew, W. Weedon, A 3D perfectly matched medium from modified Maxwell's equations with stretched coordinates, Microwave Opt. Technol. Lett. 7 (1994) 599–604.
[17] F.L. Teixeira, W.C. Chew, Systematic derivation of anisotropic PML absorbing media in cylindrical and spherical coordinates, IEEE Microwave Guided Wave Lett. 7 (1997) 371–373.
[18] F.L. Teixeira, W.C. Chew, Analytical derivation of a conformal perfectly matched absorber for electromagnetic waves, Microwave Opt. Technol. Lett. 17 (1998) 231–236.
[19] O. Ozgun, M. Kuzuoglu, Non-Maxwellian locally-conformal PML absorbers for finite element mesh truncation, IEEE Trans. Antennas Propag. 55 (2007) 931–937.
[20] O. Ozgun, M. Kuzuoglu, Multi-center perfectly matched layer implementation for finite element mesh truncation, Microwave Opt. Technol. Lett. 49 (2007) 827–832.
[21] G.W. Milton, M. Briane, J.R. Willis, On cloaking for elasticity and physical equations with a transformation invariant form, New J. Phys. 8 (248) (2006) 1–20.
[22] S.A. Cummer, D. Schurig, One path to acoustic cloaking, New Journal of Physics 9 (45) (2007) 1–8.
[23] M. Kuzuoglu, R. Mittra, A systematic study of perfectly matched absorbers, in: D.H. Werner, R. Mittra (Eds.), Frontiers in Electromagnetics, IEEE Press, 2000.
[24] J. Jin, The Finite Element Method in Electromagnetics, John Wiley & Sons, 2002.
[25] D. Colton, Partial Differential Equations – An Introduction, Random House, New York, 1971.
[26] R.F. Harrington, Field Computation by Moment Methods, Macmillan, 1968.